Development of electron reflection suppression materials for improved thermionic energy converter performance using thin film deposition techniques

Mohammad Islam[a] and Osman T. Inal
Department of Materials and Metallurgical Engineering, New Mexico Institute of Mining and Technology, Socorro, New Mexico 87801

James R. Luke
New Mexico Institute of Mining and Technology, Institute for Engineering Research and Applications (IERA) , 901 University Blvd. SE, Albuquerque, New Mexico 87106–4339

(Received 14 February 2006; accepted 26 June 2006; published online 18 October 2006)

Nonideal electrode surfaces cause significant degree of electron reflection from collector during thermionic converter operation. The effect of the collector surface structure on the converter performance was assessed through the development of several electron reflection suppression materials using various thin film deposition techniques. The double-diode probe method was used to compare the *J-V* characteristics of converters with polished and modified collector surfaces for emitter temperature and cesium vapor pressure in the ranges of 900–2000 K and 0.02–1.5 torr, respectively. The coadsorption of cesium and oxygen with respective partial vapor pressures of ~1.27 torr and a few microtorrs reduced the emitter work function to a minimum value of 0.99 eV. It was found that the collector surfaces with matte black appearance such as platinum black, voided nickel from radio-frequency plasma sputtering, and etched electroless Ni–P with craterlike pore morphology exhibited much better performance compared with polished collector surface. For these thin films, the increase in the maximum output voltage was up to 2.0 eV. For optimum performance with minimum work function and maximum saturation emission current density, the emitter temperature was in the range of 1100–1500 K, depending on the collector surface structure. The use of these materials in cylindrical converter design and/or in combination with hybrid mode triode configuration holds great potential in low and medium scale power generators for commercial use.
 [DOI: 10.1063/1.2356785]

I. INTRODUCTION

A thermionic energy converter (TEC) is a direct energy conversion device that transforms heat into electricity with no moving parts.[1] Its operation is analogous to that of a heat engine with electrons as the working fluid. The TEC performance is adversely affected by the negative space-charge effect and the electron reflection from nonideal electrode surfaces, both of which result in loss of emission current collected at the collector surface due to electron scattering and back reflection into the plasma.[2] The performance of a TEC is assessed using barrier index voltage (V_B) as the figure of merit. The value of V_B depends on the collector work function ϕ_C, arc voltage drop V_d, and the attenuation voltage V_a such that[3]

$$V_B = \phi_C + V_d + V_a. \quad (1)$$

The adsorption of cesium lowers the work function of tungsten and nickel surfaces to minimum values of 1.52 and 1.37 eV, respectively. Small amount of oxygen coadsorbed on the cesiated refractory metal surface greatly enhances the degree of thermionic emission due to the increase in the binding energy between Cs and the W substrate. The coadsorption of oxygen also leads to further lowering of the work function to a minimum value of 1.1 eV.[4] A study carried out for iridium and lanthanum hexaboride substrates reported a minimum work function value of ~1.0 eV for simultaneous Cs–O adsorption.[5] The downside of oxygen presence during converter operation is an associated increase in the electron reflectivity from the collector surface. The higher degree of electron reflection from the collector reduces the converter output voltage, thereby increasing the barrier index voltage via an increase in the arc voltage drop V_d. The electron reflection from the collector accounts for an increase in the value of V_B by ~0.3 eV.

The degree of electron reflection depends on several features such as surface structure, chemical composition, degree of coverage of the adsorbed species, and faceting and patch effects in polycrystalline surfaces. A promising approach for electron reflection suppression is to capture the incident electrons through multiple reflections within the structure. For n number of multiple reflections, the electron reflection coefficient decreases by a factor R^n.[2] The platinum black surface, for instance, was reported to exhibit an electron reflection coefficient of ~6%–8% for low energy electron beams.[6]

In the past, the multiple modular redundancy and high heat rejection temperature capabilities gave TECs a distinct edge over conventional turboelectric systems in reliability, development cost, and system weight for aerospace use. The incorporation of recent advancements in plasma physics, sur-

[a]Electronic mail: mohammad.islam@gmail.com

face science, and hybrid mode triode design predicts an increase in conversion efficiency to ~23%,[7] making this technology feasible for applications such as hybrid systems for cogeneration, stand-alone power generators, and power plant toppings.

In this paper, the effects of different surface structures on electron reflection from the collector are reported. Using plasma-assisted physical vapor deposition and electrochemical plating processes, thin films with different surface morphologies were obtained on the collector surface. These films were characterized for chemical composition and surface and cross-sectional morphologies to develop an understanding of the relationship between film synthesis parameters and the resulting film characteristics. Using the double-diode probe method under identical operating conditions, the performance of the converters with polished and modified collector surfaces was compared for a range of emitter temperatures and icesium vapor pressures.

II. EXPERIMENTAL PROCEDURE

A. Thin film synthesis and characterization

The substrates were 0.6 mm thick nickel coupons, 4 $\times 5$ mm^2 in size, with surface roughness of 0.1 μm or less. After washing and drying with inert pressurized air, the surfaces were cleaned ultrasonically first in acetone and then in methanol for 5 min each to remove organic residues and surface impurities. Immediately after that, the substrates were used for thin film synthesis.

The nickel films were deposited at different conditions of the working gas pressure and the radio-frequency (rf) power using an unbalanced rf plasma magnetron sputtering unit. The system consisted of a stainless steel chamber with a planar 2 in. diameter sputter target assembly with stacking of rare-earth magnets at the back. The unbalanced magnetic field configuration increases the sputtering yield and ensures ignition of stable plasma at very low chamber pressures. A very high vacuum level was attained using a turbo-molecular pump with backing mechanical pumps. For the film deposition, the plasma was ignited and sustained using a 555 W rf generator with an automatic matching network. The substrate temperature, argon flow rate, and the substrate-to-target distance were kept the same at their respective values of 298 K, 10 SCCM (SCCM denotes cubic centimeter per minute at STP), and 10 cm for all the deposited films. The applied rf power, chamber pressure (p), and deposition time (t) were the only parameters varied to obtain nickel films with different surface morphologies.

For electroless nickel plating, the precursor solution was procured from Alfa Aesar (CAS No. 44215-K2). The substrates were immersed in the plating bath solution at 348–363 K for different times. After the deposition, the samples were rinsed with de-ionized water and dried with inert pressurized gas. Some of the deposited electroless nickel films were etched in concentrated nitric acid to modify the surface morphology. The platinum black surfaces were obtained using an aqueous solution of 0.072M chloroplatinic acid and $3.5\times 10^{-4}M$ lead acetate in a commercially available electrodeposition unit. Another sample was prepared by sand blasting the polished nickel surface for 30 s. Table I lists the processing conditions for all the electron reflection suppression materials (ERSMs) prepared for this study. In this paper, the different types of collector surfaces such as polished nickel, sputter deposited nickel, platinum black, as-deposited, and etched electroless Ni–P films are referred to as p-Ni, RF, Pt, EN-a, and EN, respectively.

TABLE I. Sample identification and processing conditions for electron reflection suppression materials (ERSMs).

ID	Plasma sputtered	ID	Electroless Ni
RF1	50 W, 2 μtorr, 0.5 h	EN1-a	80 ml, 353–358 K, 1.0 h
RF2	100 W, 2 μtorr, 2.0 h	EN2-a	80 ml, 353–358 K, 2.0 h
RF3	100 W, 20 μtorr, 0.5 h	EN2	5.33M HNO_3, 4.0 min, 338 K
RF4	100 W, 20 μtorr, 2.0 h	EN3-a	80 ml, 353–358 K, 3.0 h
RF5	200 W, 2 μtorr, 2.0 h	EN3	5.33M HNO_3, 4.0 min, 338 K
RF6	200 W, 20 μtorr, 2.0 h	EN4-a	80 ml, 353–358 K, 4.0 h
		Others	
SB	Sand blasting, 30 s	RF1-SB	Sand blasting,
Pt1	30 mA, 1.0 min		50 W, 2 mtorr, 0.5 h

The films were characterized for thickness, deposition rate, and surface and cross-section microstructures to examine the effect of synthesis parameters on the film characteristics. The surface morphology of the films was examined using scanning electron microscope (SEM) (JEOL6100). Prior to the SEM examination, the films were coated with a 15–20 nm thick conductive gold layer. The chemical composition of the as-deposited and etched electroless nickel films was determined using x-ray diffractometer (Siemens Kristalloflex 8100). The film thickness measurements were made on the samples with partially exposed substrate to obtain average step height using surface profilometer (DEKTEK III, Veeco Metrology Group).

B. Thermionic energy conversion testing

A cold seal test tube design containing the double-diode probe assembly was used for thermionic conversion testing. A biporous nickel wick was used to ensure continuous supply of the cesium and oxygen vapor into the interelectrode region. The temperature gradient along the wick gives rise to differential Cs–O vapor pressure at its ends. Thus, it is possible to have Cs–O vapor pressure of the order of ~1 torr at the hot end and few microtorrs at the cold wick end. The liquid Cs–O evaporates at the hot end into the interelectrode space, from where the gradient in vapor pressure causes transport to, and the subsequent condensation of, the Cs–O vapor at the cold wick end. From there, the capillary action channels the liquid Cs–O back to the hot wick end via small pores. The wick not only enables continuous supply of the Cs–O vapor into the interelectrode space due to its unique functionality but also allows incorporation of an internal Cs reservoir with cold seal insulator at the end of test tube, thus eliminating the issues associated with fabrication, operation, and maintenance of the converter system with an external Cs source. Using the wick also resolves the problem of O consumption by high temperature structural components during TEC operation.

TABLE II. TEC test conditions for double-diode probe method. Data for converters with *p*-Ni collector were obtained under operating conditions identical to those with ERSMs.

	T_E effect				p_{Cs} effect				
ID	T_E (K)	T_C (K)	T_w (K)	p_{Cs}, p_O	T_E (K)	T_C (K)	T_w (K)	p_{Cs}	p_O (μtorr)
SB	1296–2010	465–494	554	1.1 torr, 4.3 μtorr	1385–1612	421–503	438–553	17.1 mtorr–1.1 torr	1.4–23.5
Pt1	1227–1891	506–562	563	1.4 torr	1304–1571	505–624	457–563	39.1 mtorr–1.4 torr	0.3–7.1
RF1–SB	···	···	···	···	1217–1492	495–555	458–568	40.7 mtorr–1.6 torr	0.5–16.3
RF2	955–1875	611–652	563	1.4 torr	813–922	499–806	403–563	3.1 mtorr–1.4 torr	1.1–7.5
RF6	930–1918	433–485	563	1.4 torr	1269–1322	426–451	433–573	13.6 mtorr–1.8 torr	···
EN3–a	1056–1910	561–621	566	1.5 torr	1136–1363	470–575	418–564	6.6 mtorr–1.4 torr	···
EN3	1146–1830	559–615	565	1.5 torr	990–1176	466–574	453–563	33.0 mtorr–1.4 torr	0.5–0.8
EN2	841–1723	433–485	563	1.4 torr	818–1039	590–653	438–573	17.1 mtorr–1.8 torr	···

The double-diode probe used for this work was in the form of a self-heated tungsten filament emitter with nickel collectors on both sides. One of the collectors had a polished surface, whereas the other collector had specific surface features arising from mechanical or thin film synthesis treatment. The back surface of each collector was spot welded with the connecting electrical leads and the thermocouples. This configuration produced two TECs with a common emitter and facilitated acquisition of *J-V* output characteristics under exactly the same operating conditions with the only difference being the collector surface structure. The major advantage of the cold seal test tube TEC design is very little process setup time, typically ~10 min, which is very helpful for exploratory research since the conventional TECs with external Cs source require a week to outgas and startup. More details on the double-diode assembly and the test setup for thermionic conversion can be found elsewhere.[2,9] Table II presents the operating conditions for converters with different ERSMs assessed for their effectiveness against electron reflection.

1. Determination of emitter temperature (T_E)

Direct measurement of the emitter temperature T_E using a thermocouple was not possible. Also, the presence of purple plasma during the Cs discharge prevented the measurement of T_E using an optical pyrometer. The values of T_E and the emitter work function (ϕ_E), therefore, were estimated using an iterative approach that involved the measurement of T_E in the absence of plasma glow and correlating that to the power required to heat the filament. This was accomplished by using initial guessed values of T_E and ϕ_E to calculate the electron cooling power P_e using the expression[7]

$$P_e = AJ(\phi_E + 2kT_E/e). \tag{2}$$

The power to heat the emitter filament P_1 is $P_1 = I_f V_f - P_e$, where I_f and V_f were the filament current and voltage, respectively. From the Richardson equation, the value of ϕ_E that gave the observed emission current was determined and compared to the initial guess. If needed, a new value of ϕ_E was used in Eq. (2). It was found that after some iteration, the guessed values converged with the experimental values.

2. Calculation of Cs, O equivalent vapor pressures (p_{Cs}, p_O)

The value of p_O was determined using sputter recovery emission elevation (SPREE) method.[10] A 60 Hz sine wave pulse was applied for a half-cycle time of ~8 ms with maximum intensities of 20–30 V to remove the adsorbed oxygen having a sputtering threshold value of 7.5 eV for O removal by Cs^+ ions. Although the applied sputtering pulse removes both adsorbed Cs and O, the readsorption of Cs to the emitter surface takes place immediately, whereas the O coverage is restored gradually. This is due to the large difference in arrival rates of Cs and O caused by much higher partial vapor pressure of Cs compared with that of O. The large difference in arrival rates of Cs and O makes it possible to measure p_O in Cs–O vapor since the increase in emission current over time is directly proportional to the degree of emitter surface coverage by the coadsorbed O. The relative values of emission current at T_E immediately after the sputtering pulse is stopped and after time t can be used to determine p_O,[8]

$$p_O = 1.7 \times 10^{-10} T_E \ln(I/I_0)/t. \tag{3}$$

In pure phase form, the liquid Cs reservoir temperature T_R and the corresponding vapor pressure p_{Cs} are related according to the equation[1]

$$p_{Cs} = 2.45 \times 10^8 (T_R)^{-1/2} \exp(-8910/T_R). \tag{4}$$

The source of oxygen during TEC operation was residual oxygen in the system. In the absence of a dedicated, particular source of oxygen, it is believed that the amount of oxygen in the system was very low, typically ~10^{-6}–10^{-7} torr, as confirmed from p_O calculation using the data obtained. The value of p_{Cs}, therefore, was assumed to be equal to that of pure Cs in the system and was determined using Eq. (4).

III. RESULTS AND DISCUSSION

A. Film characterization

1. Plasma magnetron sputtered films

For all the films, the homologous temperature T/T_m (T and T_m are substrate temperature and melting temperature for nickel, respectively) of 0.174 belongs to the regime where the microstructure of the film depends on a plethora of pa-

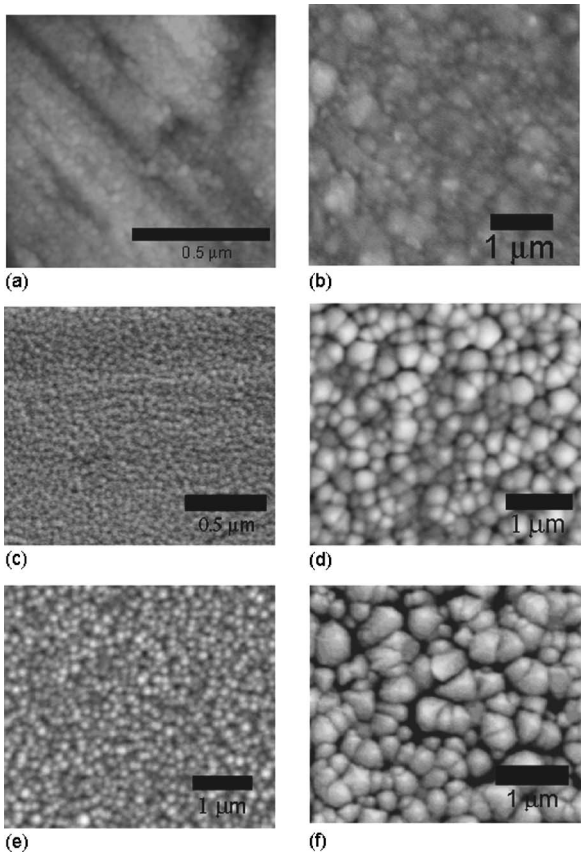

FIG. 1. SEM microstructures of the rf plasma sputtered nickel films prepared under different deposition conditions (Table I): (a) RF1, (b) RF2, (c) RF3, (d) RF4, (e) RF5, and (f) RF6.

rameters such as apparatus configuration, substrate surface morphology, and working gas pressure, all of which influence arrival directions, energy, and momentum delivered to the substrate by the sputtered and/or other energetic bombarding species.[10] Therefore, films with very different characteristics were obtained by varying the processing parameters. The microstructures of the film surfaces obtained from SEM studies are shown in Fig. 1.

The films had shiny mirrorlike, gray, or matte black surfaces depending on the deposition pressure (p). Beyond transition pressure p_t, the high incidence of gas scattering of the sputtered species causes oblique component in the deposition flux of arriving particles.[11] The films RF2, RF4, RF5, and RF6 exhibited open, voided structure representative of the zone I of the structure zone model (SZM).[12] For the same value of p, an increase in the applied power resulted in a decrease in p_t as manifested by the ability to obtain films with dark visual appearance at chamber pressures as low as 2 mtorr and 200 W power. It is possible that atomic shadowing during transport was caused by high sputtering yield at higher power and resulted in a large degree of collisional scattering by inert gas molecules.[13] On the other hand, the films RF1, RF1-SB, and RF3 exhibited mirrorlike surface topography characteristic of the dense zone T structure. The low p minimizes the oblique component in the deposition flux and hence very smooth films were obtained with crystal structures that appeared fibrous and were difficult to resolve. For the same power and deposition time, increasing the pressure from 2 to 20 mtorr increased the average crystallite size from ~89 to ~366 nm, as evident from Figs. 1(b) and 1(d). The same trend followed in the cases of RF5 and RF6, where high pressure increased the average crystal size from ~103 to 390 nm. The increased pressure also decreased the film deposition rate due to reduction in the mean free path of the gas atoms with corresponding increase in the collisional scattering events. This finding is apparently in contrast with the earlier result where, for the same input power, a decrease in grain size with increasing argon gas pressure was reported.[14] This contradiction may be attributed to the lateral grain growth caused by increased surface mobilities of the adatoms due to the substrate heating at high input rf power and for longer deposition time.

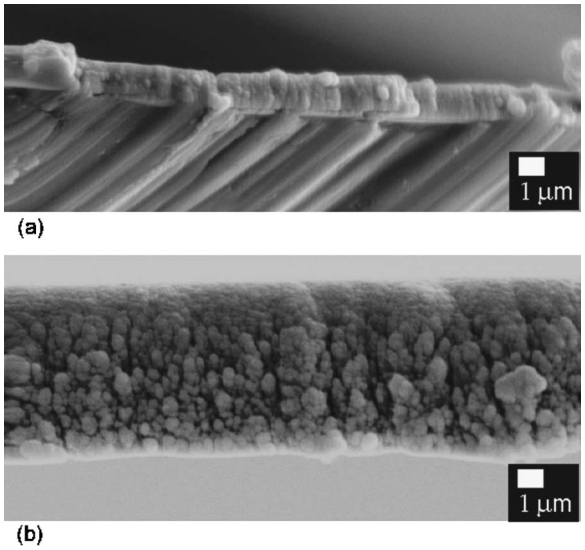

FIG. 2. Scanning electron microscope images of the rf plasma sputtered nickel film cross sections: (a) RF2 (100 W, 2 mtorr, 2.0 h) and (b) RF5 (200 W, 2 mtorr, 2.0 h).

The comparison of RF2–RF5 and RF4–RF6 indicates the effect of power on the average crystal size, although this effect was not as large as that of the chamber pressure. The effect of applied power on the thickness and growth morphology of the deposited films is demonstrated by the cross-sectional view of the RF2 and RF5 films in Fig. 2. It was found that increasing the applied power by a factor of 2 changed the growth morphology from columnar to granular along with significant increase in porosity level in the film. This may be due to a transition in the nature of arriving flux at the substrate surface caused by the higher sputtering yield at higher applied power levels.

2. Electroless nickel films

The SEM studies of the as-deposited nickel-phosphorus films revealed smooth surface morphology with a slight increase in average surface roughness for longer deposition times. This may be attributed to the grain growth during the deposition process promoted by the surface adatom mobilities. This is also supported by reduced porosity level seen in the films obtained from longer deposition times, as shown in Figs. 3(a)–3(c). The film characteristics for sputtered nickel and as-deposited electroless Ni–P films are listed in Table III.

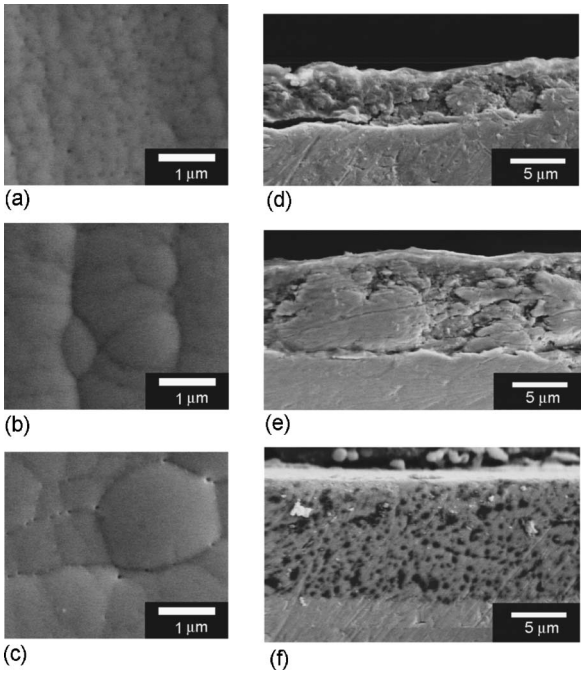

FIG. 3. High magnification view of the as-deposited electroless Ni–P films (Table I): surface morphologies of (a) EN1-a, (b) EN2-a, and (c) EN3-a, and film cross sections for (d) EN1-a, (e) EN2-a, and (f) EN4-a samples.

The cross-sectional SEM studies of the samples revealed granular morphology of the films. From the SEM images shown in Figs. 3(d)–3(f), the respective values of average film thickness for these samples were found to be ~4.81, 8.23, and 11.0 μm with corresponding growth rates of 802, 686, and 457 Å/min, respectively. The gradual decrease in the deposition rate over time indicated depletion of nickel ions in the precursor solution. The acid treatment of the metallic, semibright films progressively transformed them into black spectrally selective surfaces. The matte black appearance of the films arises from selective etching of the Ni–P film to form a porous network. Different etching treatments produced pores with strikingly different pore structures, as shown in Fig. 4. The craterlike and stalagmite morphologies are caused by different etching rate for different alloy compositions of the deposited Ni–P films. The former is obtained due to higher etching rate of nickel when P content in the film is very low (typically, less than 8 wt %).[15]

TABLE III. Characteristics of electron reflection suppression materials (ERSMs) as determined from SEM and surface profilometry.

ID	Crystal size	Thickness (μm)	Rate (Å/min)
RF1	21.3 nm		
RF2	85.0 and 30.0 nm	1.54	129
RF3	32.9 nm	1.05	350
RF4	366 and 139 nm	3.55	296
RF5	103 nm	7.11	592
RF6	388 and 158 nm	3.68	307
EN1-a	0.28 μm	4.81	802
EN2-a	1.31 μm	8.23	686
EN4-a	1.08 μm	11.0	457

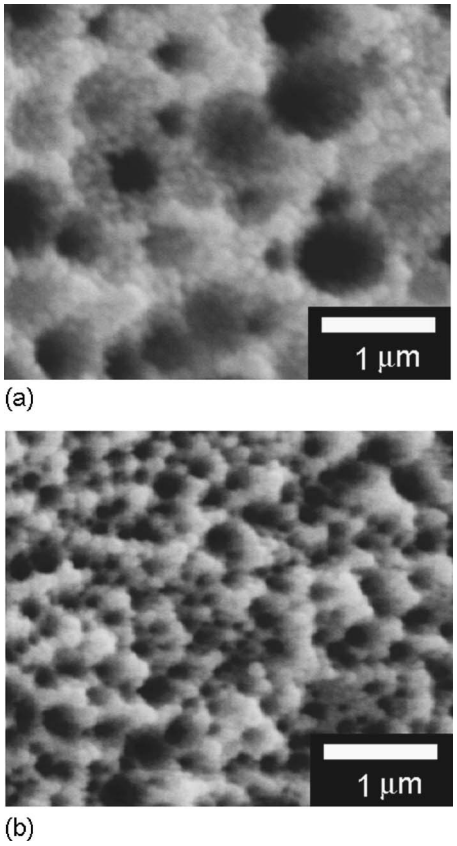

FIG. 4. Different pore structures formed as a result of acid treatment of the as-deposited electroless Ni–P films: (a) crater morphology (EN2) and (b) stalagmitelike morphology (EN3).

The x-ray diffraction scans of the as-deposited and etched films revealed a gradual decrease in the nickel content and the appearance of the Ni–P phases in the films for longer deposition times and from etching treatment, as indicated in Fig. 5(a). The as-deposited films were highly crystalline with the presence of peaks from pure nickel and the Ni–P phases such as $Ni_{2.55}P$, Ni_5P_2, $Ni_{12}P_5$, and NiP_2. The peak intensities for Ni–P phases increased with corresponding decrease in those for pure nickel. The low P content in the films resulted in crystalline film structure with very well-defined and sharp peaks. It is an established fact that the as-deposited electroless Ni–P films are microcrystalline or completely amorphous in nature.[16] The solution composition leading to fast nickel deposition and low phosphorus codeposition rate, together with substrate temperature high enough to promote surface diffusion due to high adatom mobilities, may have caused high level of crystallinity in the deposited films. The location and change in intensities of some of the peaks such as those at 2θ values of ~51.6° 76.2°, and 92.7° suggest the possibility of overlap between peaks characteristic of pure nickel and some Ni–P phase. Etching the deposited films increased the intensity of the peaks located at 2θ values of ~50.1° and 76.3°, as shown in Fig. 5. These results indicate chemically selective nature of the acid etch treatment via preferential dissolution of the nickel and higher residual surface phosphorus content after etching.

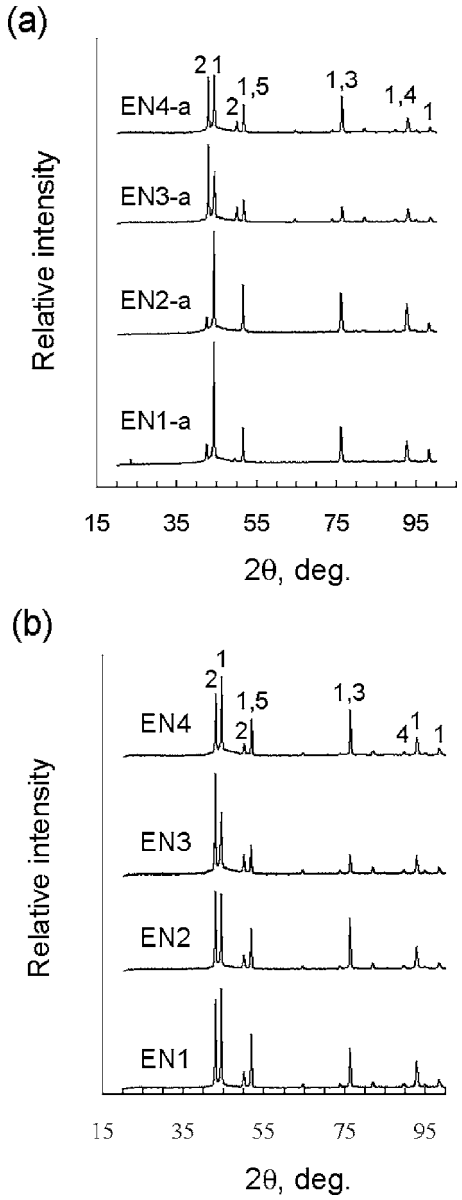

FIG. 5. X-ray diffraction spectra of the electroless Ni–P films obtained from different deposition times (a) before and (b) after acid treatment. The peaks 1–5 are characteristic of pure nickel, $Ni_{2.55}P$, Ni_5P_2, $Ni_{12}P_5$, and NiP_2 phases, respectively.

3. Platinum black film

The SEM examination of the platinum black surface revealed the presence of very fine grains with extensive agglomerate formation, thus producing a certain degree of surface nonuniformity. Such a surface morphology arises from inhibited nucleation and growth of platinum deposits due to the presence of lead acetate in the electroplating solution. From the SEM microstructure shown in Fig. 6, the average sizes of the crystallites and the agglomerates were found to be ~175 nm and 1.6 μm, respectively. The surface scratches from the substrate preparation step enhance the irregularity profile due to variations in local current density at the high and shallow regions of the substrate during the electroplating process.

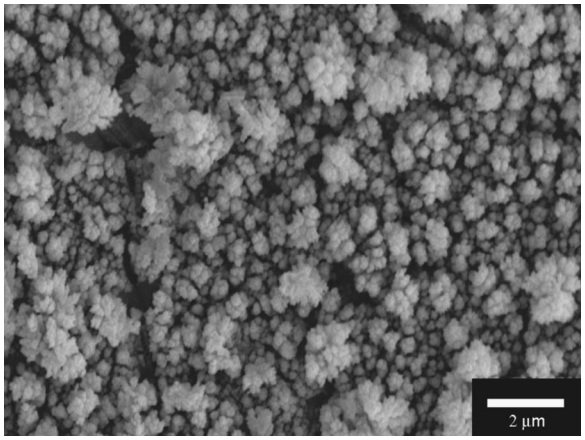

FIG. 6. SEM microstructure of the platinum black surface (Pt1).

B. Double-diode Cs–O TEC testing

The effects of emitter temperature and Cs vapor pressure on the converter output performance were examined for the collector surfaces modified with various ERSMs. The conditions of thermionic energy conversion such as emitter temperature (T_E), collector temperature (T_C), wick temperature (T_w), and equivalent partial vapor pressures of cesium (p_{Cs}) and oxygen (p_O) are listed in Table II.

1. Emitter temperature (T_E) effect

The shape of the output J-V characteristics depends, to a great extent, on two main parameters: (a) the product of Cs vapor pressure and interelectrode space, a parameter often referred to as pressure spacing ($p_{Cs}d$), and (b) the degree of space-charge neutralization indicated by the ratio of Cs^+ ions with respect to the electrons in the interelectrode space, generally defined as the ion richness ratio (β). For our TEC design, the values of d and T_w for the tested range of emitter temperatures were 0.75 mm and 555–563 K, respectively. The testing for thermionic conversion was carried out for the p_{Cs} value somewhere in the range of ~1.0–1.5 torr with a corresponding $p_{Cs}d$ value of ~30–40 mtorr. Thus, the system always operated as a high pressure Cs vapor plasma converter. The graphical representation of the data obtained at different T_E values for various ERSMs is given in Fig. 7. The general trend seen was a gradual increase in the output current density to a maximum value followed by a decrease at higher T_E values. The increase in the maximum current density for a particular T_E value was accompanied by a corresponding decrease in the maximum output voltage. For a given cesium vapor pressure, the increase in T_E initially leads to increased emission current density to a maximum value with minimum ϕ_E value, followed by a decrease due to a decrease in the cesium coverage and finally starts to rise again as T_E becomes very high. The higher value of the maximum output voltage at elevated temperatures is attributed to the larger kinetic energy of the emitted electrons as well as changes in the ionization and recombination processes that result in a lower Cs plasma density.[17]

The effect of emitter temperature on the maximum output current density and the emitter work function values for different types of modified surfaces is presented graphically

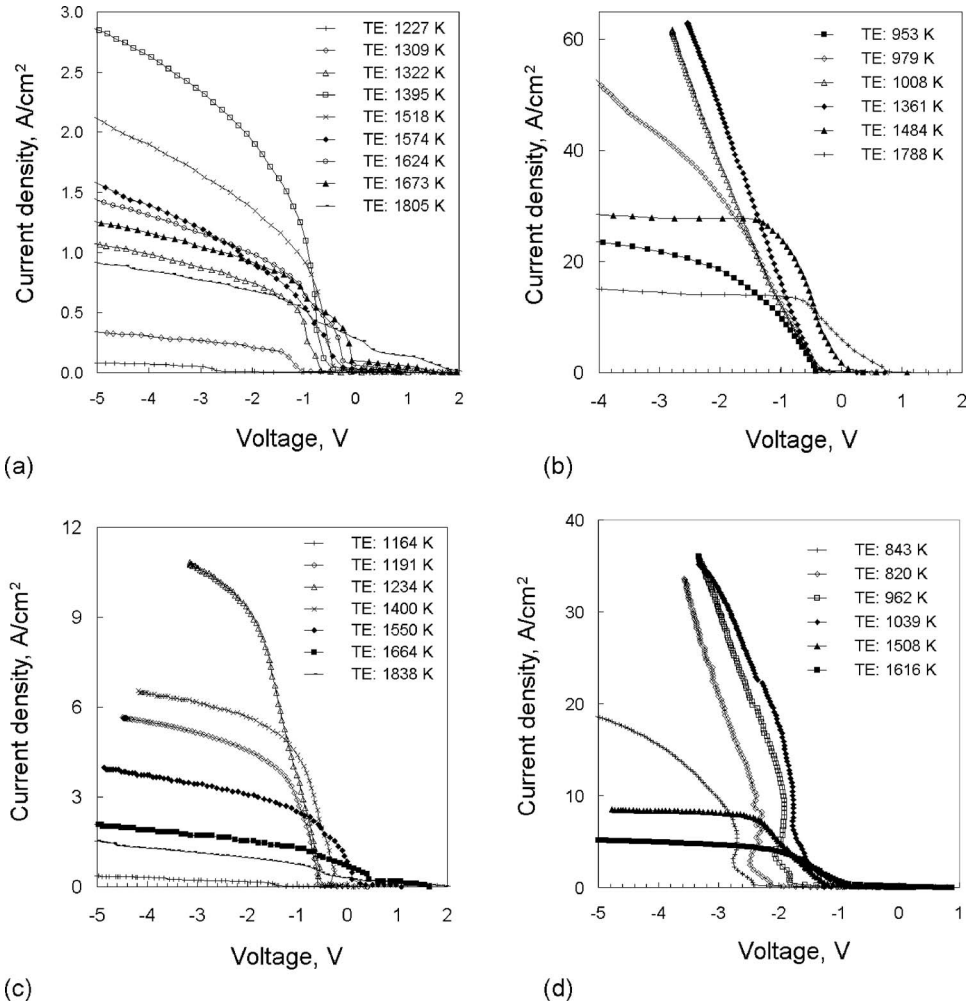

FIG. 7. *J-V* output characteristics over a range of emitter temperatures (T_E) for TECs with different collector surface structures: (a) platinum black (Pt1), (b) rf plasma sputtered nickel (RF2), (c) rf plasma sputtered nickel (RF6), and (d) etched electroless Ni–P (EN2).

in Fig. 8. These data are a subset of the S-shaped curves for higher cesium reservoir temperatures that were developed by Houston and Webster[9] through extrapolation of the theoretical work by Taylor and Langmuir.[18] It is interesting to note that the output current density for the RF2 sample shoots to a maximum value at much lower emitter temperature. Also, the maximum current density was higher than the rest of the samples by two to three orders of magnitude. Since the supply of oxygen during converter operation was not controlled, but rather depended on the residual oxygen in the system, it is very likely that the Cs–O mixed vapor composition in this case was significantly different during thermionic conversion testing. Thus, the Cs–O coadsorption to the emitter surface resulted in reduction in the emitter work function value to a greater extent with a corresponding increase in the thermionic emission current.

The difference in the output voltage between the thermionic converters with polished nickel (*p*-Ni) and modified collector surface was determined for the tested range of emitter temperatures in case of each ERSM. It was noticed that both extremely smooth as well as macroscopically rough surface structures did not exhibit any significant improvement in converter performance over the polished nickel collector. The collectors with sand-blasted surface, dense smooth sputtered nickel films, and as-deposited electroless nickel films fall in this category. The surfaces with certain degree of

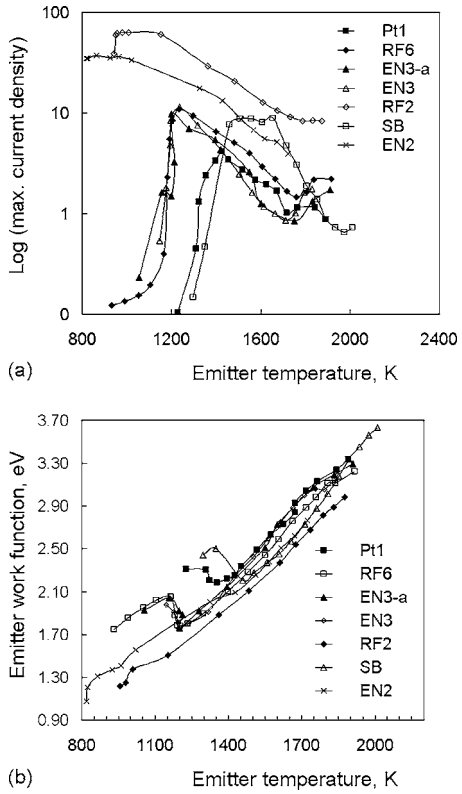

FIG. 8. Emitter temperature dependence of the output parameters during converter operation: (a) maximum saturation emission current density (J_s) and (b) emitter work function (ϕ_E).

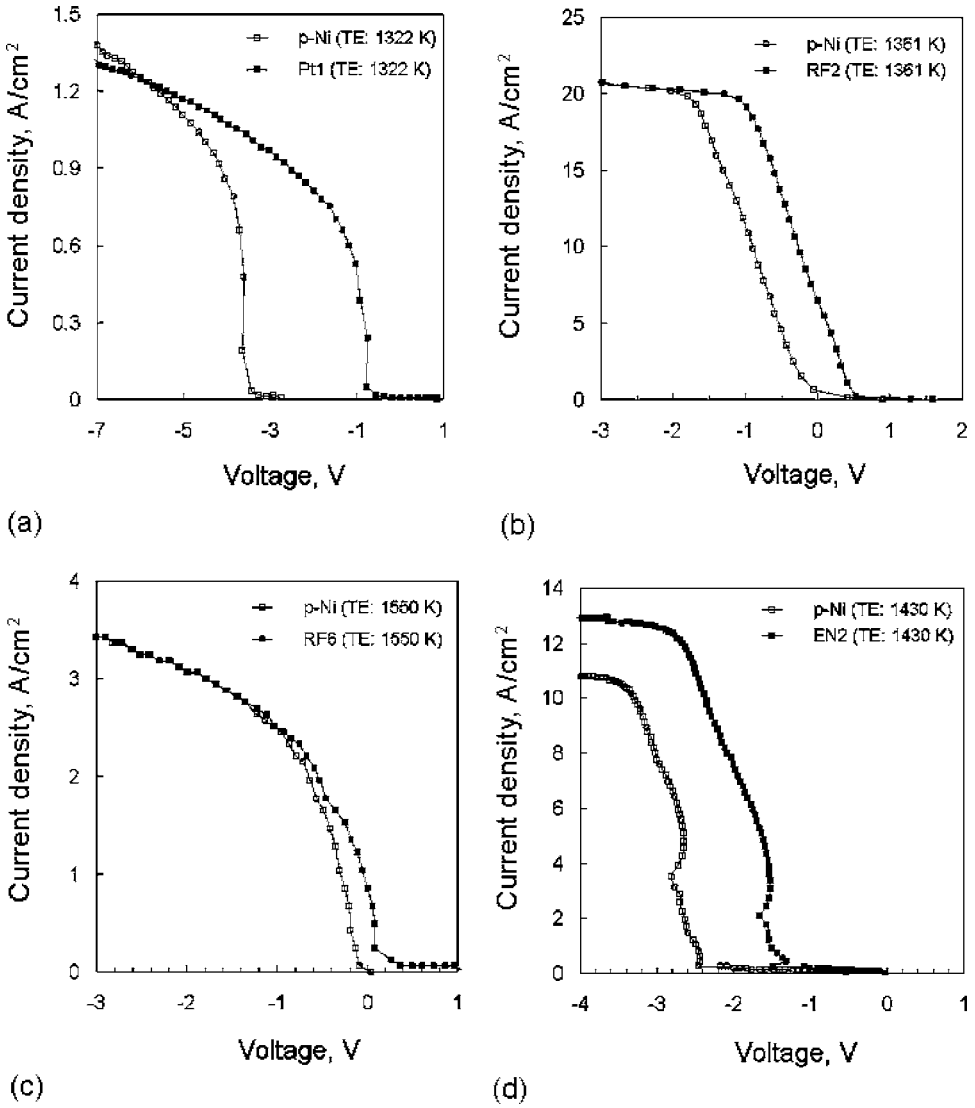

FIG. 9. Comparison of the output voltage from the converters with polished and modified collectors at specific emitter temperatures: (a) platinum black (Pt1), (b) rf plasma sputtered nickel (RF2), (c) rf plasma sputtered nickel (RF6), and (d) etched electroless Ni–P (EN2).

roughness arising from particle agglomeration, porosity formation, or voided, columnar growth indicated varying degree of improvement in the TEC performance. For such surface morphologies, the difference between polished and modified collector surfaces is depicted in Fig. 9 through the J-V output curves for both types of converters at selected emitter temperatures. For the ERSMs such as Pt1 and RF2, significant improvement in converter performance over polished collector surface was observed over the entire range of emitter temperatures. The difference in the maximum output voltage was as high as 2.03 and 0.69 V for Pt1 and RF2, respectively [Figs. 9(a) and 9(b)]. Other surfaces such as RF6 and EN2 showed mixed results with better performance at particular set of operating conditions. Both types of surfaces indicated suppression of the electron reflection through a noticeable increase in the output voltage, typically ~0.1–0.4 V, for the emitter temperature in the range of 1400–1700 K. Although in this T_E range, the value of emitter work function increased from 2.0 for EN2 and 2.1 eV for RF6 at T_E=1400 K to their respective ϕ_E values of ~2.5 and 2.9 eV at $T_E \approx 1750$ K, the better TEC performance for modified collector surfaces was mainly due to less degree of electron reflection. The assessment of each ERSM in terms of improvement in the converter performance over the polished nickel collector was done for the range of T_E tested, as shown graphically in Fig. 10. It is evident that the converter with the platinum black collector produced maximum improvement in the output performance. Table IV lists the range of output data in terms of

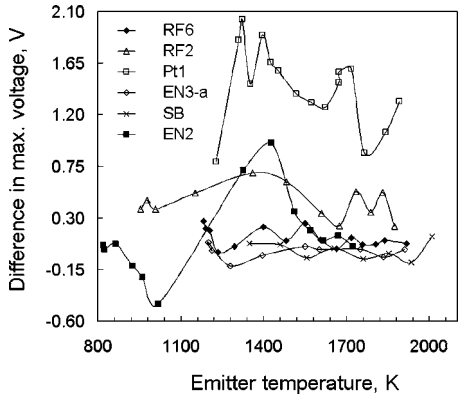

FIG. 10. Effect of the different electron reflection suppression materials (ERSMs) on the converter performance over a range of emitter temperatures in terms of change in the output voltage with respect to the converter with polished nickel collector.

TABLE IV. Emitter temperature effect: Range of values for TEC output characteristics.

ID	T_E (K)	ϕ_E (eV)	J_s (A/cm^2)	ΔV (V)
SB	1296–2010	2.21–3.63	0.15–8.89	−0.06–0.14
Pt1	1227–1891	2.19–3.34	0.10–4.12	0.79–2.03
RF2	955–1875	1.22–2.99	8.32–63.0	0.28–0.69
RF6	930–1918	1.75–3.23	0.12–10.8	0.01–0.25
EN3-a	1056–1910	1.76–3.29	0.23–9.69	−0.12–0.09
EN3	1146–1830	1.75–3.14	0.53–11.4	−0.02–0.40
EN2	841–1723	1.11–2.64	0.29–36.0	−0.45–0.95

ϕ_E, J_s, and ΔV for each ERSM assessed for its effectiveness toward suppression of electron reflection. The Cs–O mixed vapor composition during converter operation was different for one ERSM to the other due to the varying amounts of residual oxygen in the system. Also, the change in the emitter temperature influenced the Cs–O adsorption properties. Both of these factors resulted in a wide range of values for the maximum saturation emission current density and the emitter work function, typically $\sim 0.1-63.0$ A/cm^2 and $\sim 1.11-3.63$ eV, respectively. In all cases, a maximum value of the emitter work function to be less than that for the bare tungsten surface (4.52 eV) indicated the beneficial effect of Cs–O coadsorption on thermionic emission. For each ERSM, a positive value of the shift in the maximum output voltage (ΔV) indicated an improvement in the converter performance and vice versa.

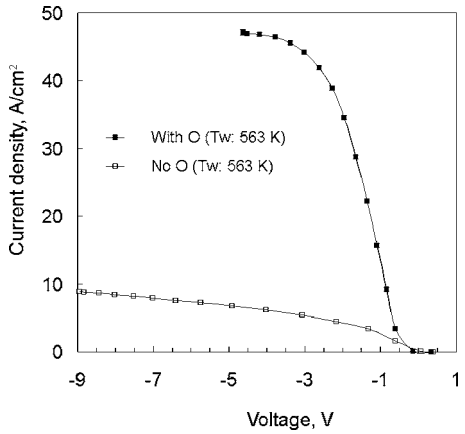

FIG. 11. *J-V* performance demonstrating the beneficial effect of oxygen coadsorption onto the cesiated emitter surface leading to enhanced converter performance.

2. Cs–O vapor pressure effect

The partial pressure of oxygen p_O is considered equivalent to the total partial pressure of all oxygen-bearing species in the Cs–O vapor because of the negligible partial pressure of free oxygen ($\sim 10^{-50}$ torr) and the presence of Cs_2O as the only significant oxygen-bearing vapor species.[19] The optimum condition of TEC operation arises from two competing effects. An increase in oxygen concentration in the Cs–O liquid increases the equivalent partial pressure of oxygen p_O in the Cs–O vapor causing maximization of the emission

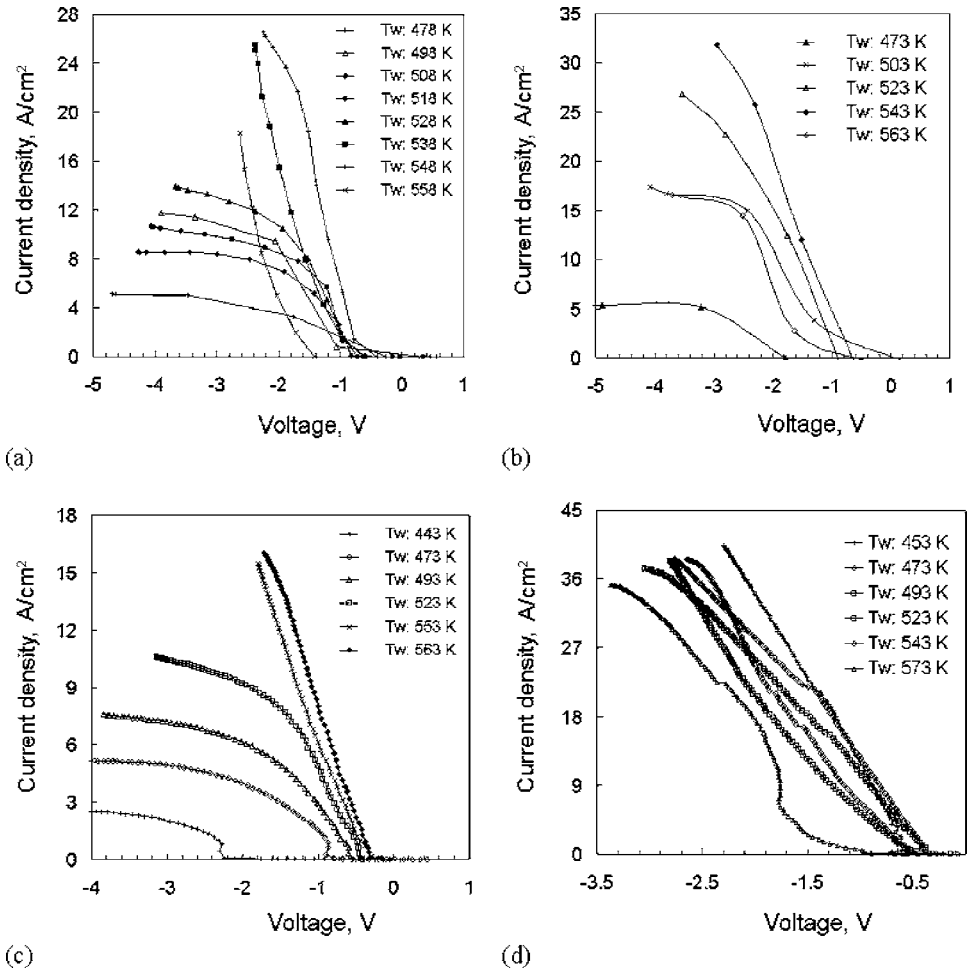

FIG. 12. Families of the *J-V* curves at different wick temperatures (i.e., the p_{Cs} values) from converters with different collector surface structures: (a) platinum black (Pt1), (b) rf plasma sputtered nickel on sand-blasted surface (RF1-SB), (c) rf plasma sputtered nickel (RF6), and (d) etched electroless Ni–P (EN2).

TABLE V. Cs vapor pressure effect: Output data range from TEC operation.

ID	T_E (K)	ϕ_E (eV)	J_s (A/cm^2)	ΔV (V)
SB	1387–1612	1.97–2.45	4.27–18.84	−0.05–0.07
Pt1	1304–1571	1.98–2.33	5.33–26.68	−0.39–1.64
RF2	813–922	0.99–1.19	69.27–116.0	0.03–0.62
RF6	1269–1316	1.90–2.09	3.05–16.22	−0.32–0.37
RF1-SB	1275–1492	1.90–2.23	5.42–32.80	0.06–0.13
EN3-a	1136–1344	1.98–2.15	0.38–7.42	···
EN3	990–1176	1.28–2.07	0.55–62.42	−0.06–0.63
EN2	818–1039	1.10–1.50	36.72–40.63	−0.33–0.89

current. As the equivalent oxygen vapor pressure increases beyond a certain value, the equivalent cesium vapor pressure decreases tending to decrease the emission current. For this study, the typical value of p_O was of the order of a few microtorrs during TEC operation. The effect of oxygen coadsorption on the emitter work function and the emission characteristics is evident from the J-V representation of the output data in Fig. 11. In this case, the initially low value of output current density due to the sputter removal of the coadsorbed Cs–O from the emitter surface was found to increase by several folds over time because of oxygen readsorption from the interelectrode region to the emitter.

The converters with various modified collector surface structures were tested for a wide range of cesium vapor pressures, dictated by changing the wick temperature, as given in Table II. Since the wick was geometrically located in close proximity to the cesium reservoir, the wick temperature T_w can be approximated to be equal to the Cs reservoir temperature T_R. Therefore, the results obtained are discussed in terms of T_w. The effect of Cs–O composition (mainly through change in p_{Cs}) was assessed by looking into the resulting output converter performance. The families of the J-V characteristics were obtained in each case. The data for some of the ERSMs, in graphical form, are presented in Fig. 12. As the Cs vapor pressure was raised by increasing the wick temperature, the Cs–O composition changed leading to the reduction in the emitter work function and consequently, a higher emission current. It was found that the saturation emission current density always maximized near or at the upper value limit for Cs vapor pressure, indicating optimum Cs–O coadsorption to the emitter surface. From the data given in Table V, the respective values of J_s for the EN2, EN3, and RF2 samples were found to be greater than other ERSMs by an order of ~2, 3, and 5, respectively. The corresponding lower values of ϕ_E indicated the reduction in emitter work function to a larger extent. These variations in the maximum saturation current density and the emitter work function values from one ERSM to the other, despite the same value of p_{Cs}, are presumably due to the variation in the residual oxygen content in each case. The change in J_s and ϕ_E as a function of p_{Cs} is expressed as the J_s-T_w and ϕ_E-T_w plots in Fig. 13. The range of output data obtained from TEC testing for p_{Cs}=0.018–1.5 torr is presented in Table V. It is believed that the relatively higher Cs vapor pressures led to enhanced emission characteristics by means of reduction in the emitter work function to a greater extent with correspondingly higher saturation emission current densities. The calculated data for J_s and ϕ_E were in the ranges of ~0.4–116.0 A/cm^2 and 0.99–2.45 eV, respectively. Although the graphical representation of data in Figs. 8(b) and 13(b) may suggest emitter work function dependence on the collector surface structure, such an implication is not true. In fact, the variation in the emitter work function for different collectors is attributed to the difference in operating conditions such as Cs–O composition, equivalent vapor pressures of Cs and O, and emitter and collector temperatures.

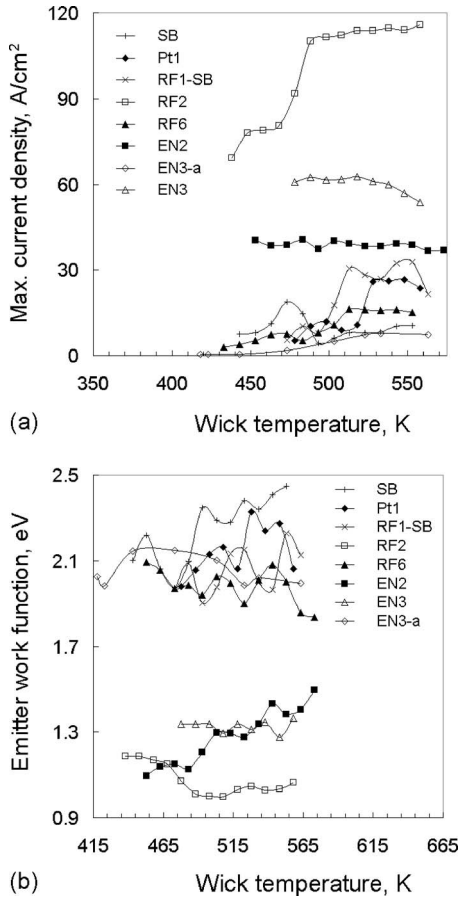

FIG. 13. Cesium vapor pressure (p_{Cs}) dependence on the converter performance: (a) maximum saturation emission current density (J_s) and (b) work function of the cesiated emitter surface (ϕ_E). The value of p_{Cs} as a function of wick temperature T_w is expressed by Eq. (4).

The converters with collector surfaces that were sandblasted, or deposited with smooth, dense rf plasma sputtered nickel, or electroless nickel films did not reduce the degree of electron reflection from the collector. These findings were consistent with the results obtained from emitter temperature effect. The TECs with Pt1, RF1-SB, RF2, RF6, and EN2 collectors produced better performance under different operating conditions. In Fig. 14, the graphical representation of J-V for polished and modified collectors at selected Cs vapor pressures underlines the importance of the collector surface structure on the suppression of electron reflection during TEC operation. The collector surface with deposited platinum black layer produced the best result, as demonstrated by the shift in the maximum output voltage to higher values. The rf plasma magnetron sputtered films also resulted in different degrees of improvement in the TEC performance.

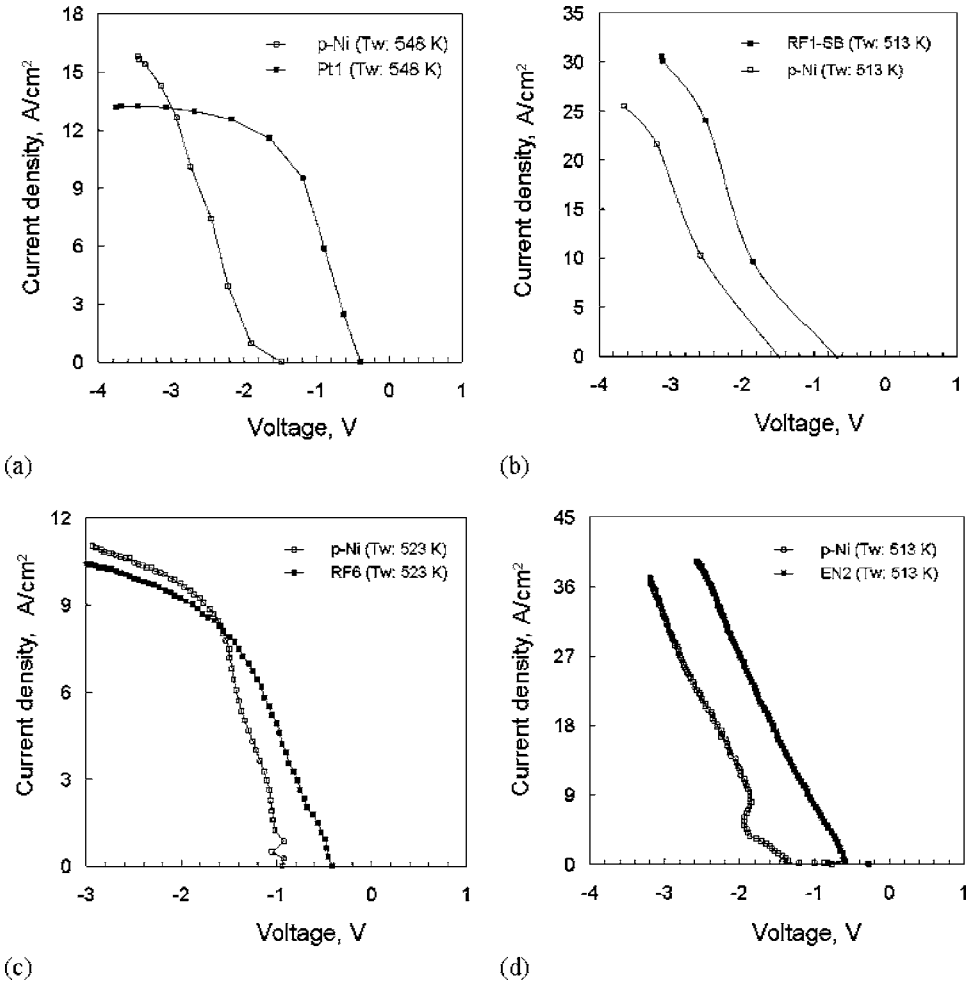

FIG. 14. Polished vs modified collector surface-TEC output for both types of converters at specific conditions of wick temperature and Cs vapor pressure: (a) platinum black (Pt1), (b) rf plasma sputtered nickel on sand-blasted surface (RF1-SB), (c) rf plasma sputtered nickel (RF6), and (d) etched electroless Ni–P (EN2).

Thus, the surface features giving rise to a certain degree of roughness, whether in the form of agglomerated crystallites as in the case of platinum black, or porous films with voided columnar growth due to oblique component in the deposition flux as obtained from rf plasma sputter deposition, or even in the shape of pores with certain morphology like in the case of etched electroless nickel films, act as trap for incoming electrons from the interelectrode region. Unlike the EN2 films with craterlike pore structure, the electroless nickel films with very smooth surface (EN3-a) as well as stalagmitelike pore morphology (EN3) did not prove to be effective against electron reflection. The shift in the maximum output voltage as a function of Cs vapor pressure is depicted graphically in Fig. 15. It was observed that although the RF2 showed better performance over the entire range of p_{Cs} values, the converter had more effective suppression of electron reflection at low Cs vapor pressures. The converse was true for converters with platinum black (Pt1) and etched electroless nickel (EN2) collector surfaces, which produced better performance for Cs pressures corresponding to T_w values of $\geqslant$493 and 493–563 K, respectively. The RF6 sample indicated improvement in converter output, though of less magnitude than RF2, at T_w in the range of 483–533 K.

IV. CONCLUSIONS

Among the several ERSMs tested, the platinum black film, rf plasma sputtered nickel films with voided, columnar growth morphology, and the etched electroless nickel with craterlike porous structure, all with matte black appearance, showed significant improvement in TEC performance. The presence of surface irregularities such as agglomerates, pores with certain morphology, or voided structures considerably reduce the degree of electron reflection. The increase in maximum output voltage by ~0.1–2.0 V suggests not only the lowering of attenuation voltage but also increase in emis-

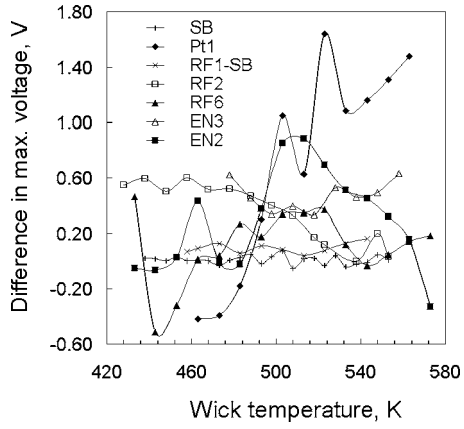

FIG. 15. Graphical representation of the shift in the maximum output voltage from the converters with different electron reflection suppression materials (ERSMs) relative to those with polished nickel collector surface. The results were obtained by operating TECs over a wide range of Cs vapor pressures adjusted through changes in the wick temperature.

TABLE VI. Optimum TEC operation characteristics for the most effective ERSMs.

ID	T_w (K)	p_{Cs}, p_O	T_E (K)	ϕ_E (eV)	J_s (A/cm^2)	ΔV (V)
Emitter temperature (T_E) effect						
Pt1	563	1.38 torr	1395	2.22	3.34	+1.89
RF2	563	1.38 torr	1151	1.51	60.2	+0.51
EN2	573	1.81 torr	1427	2.09	13.2	+0.95
Cesium vapor pressure (p_{Cs}) effect						
Pt1	523	0.43 torr, 2.92 μtorr	1571	2.33	26.0	+1.64
RF2	488	0.13 torr, 1.65 μtorr	821	1.01	110.0	+0.52
EN2	513	0.31 torr	919	1.30	39.3	+0.89

sion currents through reduction in electrode work functions through Cs–O coadsorption. The operating conditions of thermionic conversion that yielded the best performance attributes in terms of emission characteristics, together with minimum degree of electron scattering and back reflection from the collector surface, are given in Table VI. The assessment for both the emitter temperature and the Cs vapor pressure effect revealed that the most effective collector surfaces against electron reflection, in descending order, were those arising from Pt1, RF2, and EN2 films. Although the ΔV values for the EN2 sample were higher than those for RF2, the latter exhibited better performance over the entire range of T_E and at low Cs vapor pressures (i.e., low T_w values) during TEC testing, as indicated in Figs. 10 and 15, respectively. These results offer promising prospects for the development of small to medium scale power generation TEC units using Cs–O vapor plasma converters with modified collector surfaces.

The suppression of electron reflection using such surface structures in a standard TEC device such as cylindrical converter design holds great potential in lowering the value of barrier index voltage by 0.3–0.4 eV. The cold unignited plasma mode of converter operation using the hybrid mode triode (HMT) configuration warrants further lowering of the V_B value. As opposed to the ignited mode operation, this involves generation of small regions (tufts) of hot ignited plasma through ignited discharges to small anodes at the collector surface that maintain continuous supply of positive ions to the interelectrode space. The incorporation of electron reflection suppression materials (ERSMs) and the HMT design into the thermionic technology projects significant lowering of the barrier index voltage.[20] This will influence an associated increase in the energy conversion efficiency or will enable to obtain same converter performance at lower emitter temperatures. The silent, vibration-free operation of a direct power generation system as in the case of a thermionic energy converter offers potential for use in military and commercial applications such as cogeneration for domestic use,[21] power plant toppings,[22] stand-alone power generators, and high powered satellites.[23]

[1]G. N. Hatsopoulos and E. P. Gyftopoulos, *Thermionic Energy Conversion* (MIT, Cambridge, MA, 1973), p. 31.
[2]N. S. Rasor, IECEC-98–211, Colorado Springs, CO (1998).
[3]N. S. Rasor, IEEE Trans. Plasma Sci. **19**, 1191 (1991).
[4]L. Swanson and R. Strayer, J. Chem. Phys. **48**, 2421 (1968).
[5]L. R. Danielson, J. Appl. Phys. **52**, 300 (1981).
[6]R. J. Zollweg, J. Appl. Phys. **34**, 2590 (1963).
[7]J. R. Luke, IECEC-'02, Paper No. 20065, Washington, D.C. (2002).
[8]J. R. Luke, J. K. Jennings, and N. S. Rasor, Report No. JP-302101, 35 (2003).
[9]J. M. Houston and H. F. Webster, Adv. Electron. Electron Phys. **17**, 125 (1962).
[10]J. Thornton, J. Vac. Sci. Technol. A **4**, 3059 (1986).
[11]E. Kay, F. Parmigiani, and W. Parrish, J. Vac. Sci. Technol. A **6**, 3074 (1988).
[12]R. Messier, A. Giri, and R. Roy, J. Vac. Sci. Technol. A **2**, 500 (1984).
[13]P. Jouan and G. Lemperiere, Vacuum **45**, 89 (1994).
[14]M. Miller, F. Stageberg, Y. Chow, K. Rook, and L. Heuer, J. Appl. Phys. **75**, 5779 (1994).
[15]R. Brown, P. Brewer, and M. Milton, J. Mater. Chem. **12**, 2749 (2002).
[16]R. Weil and K. Parker, *Electroless Plating-Fundamentals and Applications*, edited by G. O. Mallory and H. Hajdu (William Andrews Publishing/Noyes, Norwich, NY 1990), p. 111.
[17]G. H. Gubbels and R. Metselaar, J. Appl. Phys. **68**, 1883 (1990).
[18]J. B. Taylor and I. Langmuir, Phys. Rev. **44**, 423 (1933).
[19]R. H. Lamoreaux and D. L. Hildenbrand, J. Phys. Chem. Ref. Data **13**, 151 (1984); C. F. Knights and B. A. Phillips, J. Nucl. Mater. **84**, 196 (1979).
[20]H. A. Fatmi, D. Gabor, and J. A. Nelson, International Conference on Thermionic Electric Power Generation, London, 1965, p. 1965.
[21]V. V. Klepikov, V. I. Yarygin, G. A. Kupstov, W. B. Veltkamp, and L. R. Wolff, IECEC-92, San Diego, CA, 1992, pp. 3.451–3.454.
[22]R. S. Dick, Jr., B. M. Banda and J. W. Starr, IECEC-80, Seattle, WA, 1980, pp. 21–44.
[23]G. E. Lazarenko and V. I. Yarygin, Space Nuclear Conference, Paper No. 1120, San Diego, CA, 2005.